

Asymptotic scaling laws for the stagnation conditions of Z-pinch implosions

D. E. Ruiz,^{1, a)} C. A. Williams,¹ and R. A. Vesey¹

Sandia National Laboratories, P.O. Box 5800, Albuquerque, New Mexico 87185-1186, USA

(Dated: 22 January 2025)

Implosions of magnetically-driven annular shells (Z pinches) are studied in the laboratory to produce high-energy-density plasmas. Such plasmas have a wide-range of applications including x-ray generation, controlled thermonuclear fusion, and astrophysics studies. In this work, we theoretically investigate the in-flight dynamics of a magnetically-driven, imploding cylindrical shell that stagnates onto itself upon collision on axis. The converging flow of the Z-pinch is analyzed by considering the implosion trajectory in the (A, M) parametric plane, where A is the in-flight aspect ratio and M is the implosion Mach number. For an ideal implosion in the absence of instabilities and in the limit of $A \gg 1$, we derive asymptotic scaling laws for hydrodynamic quantities evaluated at stagnation (e.g., density, temperature, and pressure) and for performance metrics (e.g., soft x-ray emission, K-shell x-ray emission, and neutron yield) as functions of target-design parameters.

I. INTRODUCTION

For many decades, pulsed-power accelerators have been used for compressing electrical energy in space and time to implode cylindrical annular shells, which are often referred as Z pinches.^{1–6} Such magnetically-driven Z-pinch implosions are studied in the laboratory to produce high-energy-density (HED) plasmas. Such plasmas have a wide-range of applications including x-ray generation,^{7–10} controlled thermonuclear fusion,^{10–15} and astrophysics studies.^{16–18} Due to the aforementioned applications, it is important to understand how the hydrodynamic conditions assembled at stagnation depend on target-design parameters of a Z pinch.

With this goal in mind, we study the idealized problem of a one-dimensional Z-pinch implosion in the absence of hydrodynamic instabilities and finite-conductivity effects.¹⁹ More specifically, we investigate the in-flight dynamics of a magnetically-driven cylindrical shell, which then stagnates onto itself upon collision on axis. The converging flow of the Z-pinch is analyzed by considering the implosion trajectory in the (A, M) parametric plane, where A is the in-flight aspect ratio (IFAR) and M is the implosion Mach number. The high-aspect-ratio limit ($A \gg 1$) is considered for most of the implosion trajectory. We then derive asymptotic scaling laws for hydrodynamic conditions evaluated at stagnation (e.g., density, temperature, and pressure) and performance metrics (e.g., x-ray emission and neutron yield) as functions of target-design parameters, specifically the implosion velocity, the liner mass per-unit-length, and the liner entropy parameter.

Understanding the pressure amplification due to converging flows has been studied before in the HED literature. In particular, this work follows the analysis presented in Ref. 20 for imploding spherical shells driven by a constant pressure source, an idealized approximation often used for modeling laser-driven HED experiments.

However, contrary to laser-driven HED experiments, the key feature of Z-pinch implosions is that the magnetic-drive pressure increases as the pinch radius decreases. This distinction introduces new subtleties to the analysis of the shell in-flight dynamics and to the estimates of the plasma conditions assembled at stagnation.

The present work is organized as follows. In Sec. II, we describe the general implosion kinematics of a Z pinch. In Sec. III, we discuss the in-flight shell dynamics of an imploding Z pinch. More specifically, we analyze how the pressure, density, thickness, and aspect ratio of the cylindrical shell evolves as it converges on axis. In Sec. IV, we derive scaling laws for the hydrodynamic quantities (e.g., density, temperature, and pressure) evaluated at stagnation. In Sec. V, we utilize the previous results to calculate the asymptotic dependencies of commonly referred performance metrics for Z-pinch applications (e.g., x-ray emission and neutron yield) with respect to target-design parameters. In Sec. VI, we discuss the results obtained. In particular, we present how the hydrodynamic quantities at stagnation and the performance metrics scale when similarity scaling Z-pinch implosions to higher currents. In Sec. VII, we summarize our results.

II. IMPLOSION KINEMATICS

We consider the temporal evolution of a magnetically-driven cylindrical liner. To describe the kinematics of a Z-pinch implosion, we model the liner as a thin shell.^{2,21–23} Under the action of an external magnetic pressure, the governing equation for the radial motion of the liner is given by

$$\hat{m} \frac{d^2 R}{dt^2} = -2\pi R P_m(t), \quad (1)$$

where $R = R(t)$ is the outer radius of the liner, \hat{m} is the liner mass per-unit-length, and $P_m(t) \doteq p_m(t, R(t))$ is the magnetic pressure evaluated at the outer surface of the liner. The liner mass per-unit-length \hat{m} is defined as

$$\hat{m} \doteq \pi \rho_0 (R_{\text{out},0}^2 - R_{\text{in},0}^2), \quad (2)$$

^{a)}Electronic mail: deruiz@sandia.gov

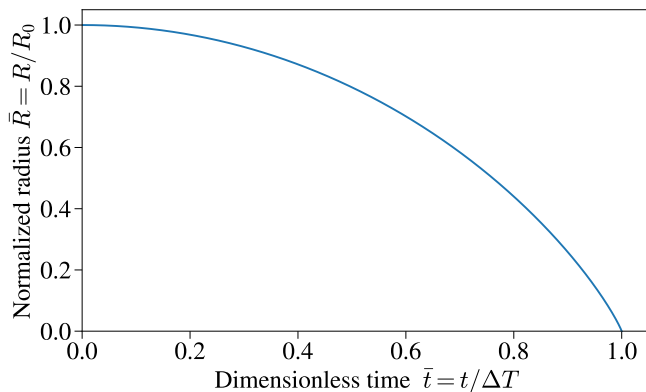


FIG. 1. Implosion trajectory of a magnetically-driven cylindrical liner driven at constant current that is initially at rest. The curve corresponds to the analytical solution in Eq. (9), and the implosion time ΔT is given by Eq. (5).

where ρ_0 is the initial mass density of the liner, $R_{\text{out},0}$ is the initial outer radius, and $R_{\text{in},0}$ is the initial inner radius. We denote $\Delta_0 \doteq R_{\text{out},0} - R_{\text{in},0}$ as the initial thickness of the liner, so the initial aspect ratio is $A_0 \doteq R_{\text{out},0}/\Delta_0$. For high-aspect-ratio liners, $A_0 \gg 1$. Thus, the mass per-unit-length can be approximated by $\hat{m} \simeq 2\pi\rho_0 R_0^2/A_0$, where we identified $R_0 \doteq R_{\text{out},0}$ for notational convenience.

In Eq. (1), the external magnetic pressure is given by

$$p_m(t, r) \doteq \frac{B_\theta^2(t, r)}{2\mu_0} = \frac{\mu_0 I^2(t)}{8\pi^2 r^2}, \quad (3)$$

where $B_\theta(t, r)$ is the azimuthal magnetic field, $I(t)$ is the electrical current passing through the shell, and μ_0 is the magnetic permeability in free space. In this work, we consider the following model for the current source $I(t)$. Prior to $t = 0$, we consider that the current has an initial “foot” stage that is large enough in amplitude to launch a shock through the liner material (see Sec. III A for more details) but small enough such that the delivered kinetic energy to the liner is negligible. After the foot stage, the current rises to its peak value I_{max} at $t = 0$ and remains constant thereafter. Up to this point, the liner motion is considered negligible so, from the perspective of the implosion kinematics, the current pulse is simply $I(t) = I_{\text{max}}$ for $t \geq 0$.^{24,25}

The implosion trajectory of the liner can be obtained by energy-conservation arguments.^{26,27} When assuming that the velocity of the liner is negligible at $t = 0$, we integrate Eq. (1) and obtain

$$\left(\frac{dR}{dt}\right)^2 = \pi \left(\frac{R_0}{\Delta T}\right)^2 \ln\left(\frac{R_0}{R}\right), \quad (4)$$

where

$$\Delta T \doteq \left(\frac{\hat{m}}{4P_m(0)}\right)^{1/2} = \left(2\pi^2 \frac{\hat{m} R_0^2}{\mu_0 I_{\text{max}}^2}\right)^{1/2}. \quad (5)$$

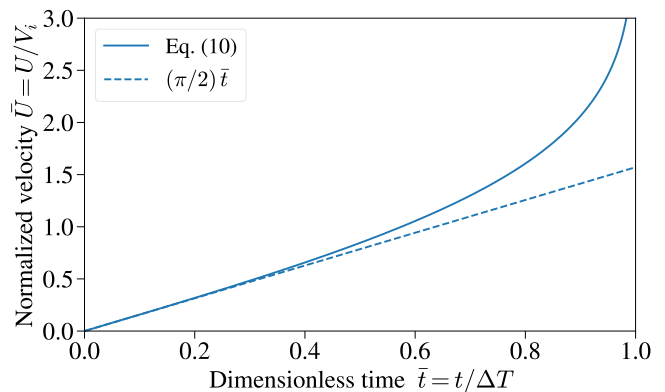


FIG. 2. Dimensionless velocity of a magnetically-driven cylindrical liner driven at constant current that is initially at rest.

When taking the negative root of Eq. (4) and integrating once more, we obtain

$$\frac{t}{\Delta T} = -\frac{1}{\sqrt{\pi}} \int_1^{\bar{R}} \frac{d\bar{R}}{\sqrt{-\ln \bar{R}}}, \quad (6)$$

where $\bar{R}(t) \doteq R(t)/R_0$ is the normalized pinch radius. The integral on the right-hand side of Eq. (6) can be written in terms of the error function:

$$\text{erf}(x) = \frac{2}{\sqrt{\pi}} \int_0^x e^{-x^2} dx. \quad (7)$$

This leads to

$$\frac{t}{\Delta T} = \text{erf}\left(\sqrt{-\ln \bar{R}}\right). \quad (8)$$

We then introduce the inverse function $\text{erf}^{-1}(x)$ of the error function $\text{erf}(x)$ such that $\text{erf}^{-1}(\text{erf}(x)) = x$. The domain of $\text{erf}^{-1}(x)$ spans $x \in (-1, 1)$ in the real line. We then obtain a closed expression for the implosion trajectory of the Z-pinch:²⁶

$$R(t) = R_0 \exp\left\{-\left[\text{erf}^{-1}\left(\frac{t}{\Delta T}\right)\right]^2\right\}. \quad (9)$$

Since $\text{erf}^{-1}(x)$ tends to infinity when its argument approaches unity, we conclude that ΔT in Eq. (5) corresponds to the implosion time of a Z pinch driven at constant current with zero initial velocity. As shown in Eq. (5), the implosion time increases for larger liner mass per-unit-length \hat{m} , larger initial radius R_0 , and smaller peak current I_{max} , as expected. For illustration purposes, the radial implosion trajectory described by Eq. (9) is shown in Fig. 1.

For the sake of completeness, we note that the obtained analytical solution in Eq. (9) can be inserted into Eq. (4) to obtain the implosion velocity as a function of time:

$$U(t) \doteq -\frac{dR}{dt} = \sqrt{\pi} \frac{R_0}{\Delta T} \text{erf}^{-1}\left(\frac{t}{\Delta T}\right). \quad (10)$$

The implosion velocity is plotted in Fig. 2. For small times $t \ll \Delta T$, U increases linearly in time; more specifically, $U \simeq (\pi/2)(R_0/\Delta T)(t/\Delta T)$. According to Eq. (10), the implosion velocity theoretically diverges to infinity as $t/\Delta T \rightarrow 1$. In reality, this does not occur due to the finite thickness of the shell, which limits the minimum radius to which current is delivered. In addition, there can be current redistribution to larger radii caused by low-density plasmas,²⁸ an effect not considered in this study.

From Eq. (10), we identify a characteristic velocity

$$V_i \doteq \frac{R_0}{\Delta T} = \left(\frac{\mu_0 I_{\max}^2}{2\pi^2 \hat{m}} \right)^{1/2}. \quad (11)$$

As expected, the characteristic velocity increases linearly with the peak current and is inversely proportional to the square root of the liner mass per-unit-length. At fixed I_{\max} and R_0 , we note that the implosion velocity scales with the square root of the liner initial aspect ratio.

III. SHELL IN-FLIGHT DYNAMICS

For Z-pinch implosions, the dynamics of the in-flight shell conditions (notably the shell pressure, density, thickness, and aspect ratio) can be decomposed into four phases. These phases are illustrated in Fig. 3 and are denoted as the (i) the magnetically-driven shock phase, (ii) the isentropic-acceleration phase, (iii) the acceleration-at-constant-shell-thickness phase, and (iv) the void-closure phase. We now discuss how the in-flight shell conditions evolve during the implosion.

A. Phase 1: Magnetically-driven shock

When a metallic liner is magnetically driven with a rapid rise in current and its thickness is sufficient for the characteristic sound waves to overlap each other within the liner, a shock wave is generated that propagates through the liner material. In metals with finite electrical conductivity, this shock wave is followed by a nonlinear magnetic-field diffusion wave, which travels at anomalously high speeds due to the increase in metal resistivity with temperature. This paper will not delve into the complex dynamics occurring during this phase; for further details, we direct the reader to Refs. 29–33.

However, one of the primary outcomes during this phase is the increase in entropy of the liner resulting from the passage of the shock wave. When the shock has broken out of the inner surface of the liner, we assume that the liner material is in an isentropic state so that the fluid density $\rho(t, r)$ and pressure $p(t, r)$ within the interior of the liner are related by $p = P_{\text{ref}}(\rho/\rho_{\text{ref}})^\gamma$. Here P_{ref} is a reference pressure, ρ_{ref} is a reference mass density, and γ is an effective polytropic index. More concretely, P_{ref} , ρ_{ref} , and γ are equation-of-state (EOS) parameters

defining the post-shock isentrope of the material conditions inside the liner. We define the entropy parameter $\alpha_{\text{ref}} \doteq P_{\text{ref}}/\rho_{\text{ref}}^\gamma$, which we assume remains constant during the implosion until stagnation.

It is worth noting that, when using an adiabatic EOS for the liner material, we are inherently ignoring energy-loss mechanisms, such as radiative losses, happening in-flight as the implosion proceeds. This effect can be important for many radiating Z-pinch experiments.³⁴

In a 1D model, the fluid momentum equation within the interior of the liner can be written as

$$\rho \left(\frac{\partial v_r}{\partial t} + v_r \frac{\partial}{\partial r} v_r \right) = - \frac{\partial p}{\partial r}, \quad (12)$$

where $v_r(t, r)$ is the radial velocity. In the high-aspect-ratio limit, we may assume a uniform acceleration of all fluid elements within the liner.³⁵ Therefore, the fluid velocity can be approximated by $v_r \simeq dR/dt$, and

$$\rho \frac{d^2 R}{dt^2} = - \frac{\partial p}{\partial r}. \quad (13)$$

When substituting $p = P_{\text{ref}}(\rho/\rho_{\text{ref}})^\gamma$ and integrating, we find the pressure field within the liner:^{36,37}

$$p(t, r) = P_m(t) \left(1 + \frac{r - R}{\Delta} \right)^{\gamma/(\gamma-1)}, \quad (14)$$

where the liner in-flight thickness is given by

$$\Delta(t) = \Delta_0 \frac{\gamma}{\gamma-1} \frac{\rho_0 R_0}{\rho_{\text{ref}} R(t)} \left(\frac{P_{\text{ref}}}{P_m(t)} \right)^{1/\gamma}. \quad (15)$$

Here we considered the region $r < R - \Delta$ as void with null pressure. Also, R corresponds to the outer liner surface, and the pressure there is equal to the magnetic pressure $P_m(t)$. When using the EOS $p = P_{\text{ref}}(\rho/\rho_{\text{ref}})^\gamma$, we obtain the density profile across the liner:

$$\rho(t, r) = \rho_{\text{ref}} \left(\frac{P_m}{P_{\text{ref}}} \right)^{1/\gamma} \left(1 + \frac{r - R}{\Delta} \right)^{1/(\gamma-1)}. \quad (16)$$

Let us now parameterize the dynamics of the imploding cylindrical shell in terms of five dynamical variables: the liner outer radius $R(t)$, the liner velocity $U(t) \doteq -\dot{R}$, the liner pressure $P(t) \doteq p(t, R) = P_m(t)$ evaluated at the outer surface, the liner density $D(t) \doteq \rho(t, R)$ at the outer surface, and the liner in-flight thickness $\Delta(t)$. Following Ref. 20, we can construct two dimensionless parameters from the five variables (R, U, P, D, Δ) . These are the liner in-flight aspect ratio $A(t)$ and the liner Mach number $M(t)$, which are defined as

$$A(t) \doteq \frac{R(t)}{\Delta(t)}, \quad M(t) \doteq \frac{U(t)}{C(t)}. \quad (17)$$

Here $C(t)$ is the characteristic sound speed within the liner and is given by

$$C(t) \doteq \sqrt{\gamma P(t)/D(t)}. \quad (18)$$

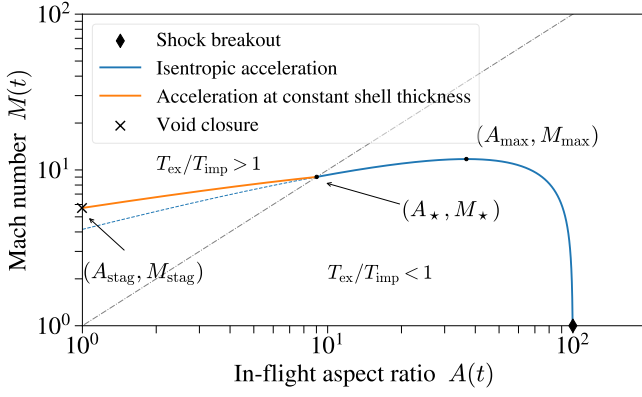


FIG. 3. Example of an implosion trajectory of a magnetically-driven cylindrical liner in the (A, M) parametric plane. In this example, we consider $A_{\text{sb}} = 10^2$ and $\gamma = 5/3$. The shock breakout point is plotted at $M_{\text{sb}} = 1$. We emphasize that the mathematical analysis presented in this work is an asymptotic theory valid in the high-aspect-ratio limit when $A(t) \gg 1$. It is worth mentioning that high-aspect-ratio implosions of aluminum foils with $A_0 \sim \mathcal{O}(10^3 - 10^4)$ have been experimentally and numerically studied at MA-scale pulsed-power machines.^{38–44}

Based on these two dimensionless quantities, the liner in-flight dynamics can be described by trajectories in the (A, M) parametric plane,²⁰ as shown in Fig. 3.

To finalize this section, we consider that the liner IFAR A_{sb} at shock breakout is known, where the “sb” subscript denotes quantities evaluated at shock breakout. Since the kinetic energy of the liner is negligible, we have $M_{\text{sb}} \simeq 0$. Upon using Eqs. (2), (3), and (15), we find the following relationships:⁴⁵

$$P_{\text{sb}} \simeq \frac{\mu_0 I_{\text{max}}^2}{8\pi^2 R_0^2} = \frac{\hat{m}}{4\Delta T^2}, \quad (19a)$$

$$D_{\text{sb}} = \rho_{\text{ref}} \left(\frac{P_{\text{sb}}}{P_{\text{ref}}} \right)^{1/\gamma} = \frac{P_{\text{sb}}^{1/\gamma}}{\alpha_{\text{ref}}^{1/\gamma}}, \quad (19b)$$

$$\Delta_{\text{sb}} = \Delta_0 \frac{\gamma}{\gamma - 1} \frac{\rho_0}{D_{\text{sb}}}, \quad (19c)$$

$$A_{\text{sb}} \simeq \frac{R_0}{\Delta_{\text{sb}}} = A_0 \frac{\gamma - 1}{\gamma} \frac{D_{\text{sb}}}{\rho_0}. \quad (19d)$$

Our next task will be to obtain a constitutive relationship between A and M for the next phases of the Z-pinch implosion shown in Fig. 3. We shall use Eqs. (19) as “initial conditions” for the in-flight dynamics.

B. Phase 2: Isentropic acceleration

The next two phases of the liner dynamics can be distinguished by considering the ratio of the following two timescales. The expansion timescale

$$T_{\text{ex}}(t) \doteq \frac{\Delta(t)}{C(t)} \quad (20)$$

measures the characteristic time for a sound wave to traverse the liner shell. In contrast, the implosion time

$$T_{\text{imp}}(t) \doteq \frac{R(t)}{U(t)} \quad (21)$$

measures the characteristic time for the change in the pinch radius. The ratio $T_{\text{ex}}/T_{\text{imp}}$ can be written in terms of the liner IFAR and Mach number as follows:²⁰

$$\frac{T_{\text{ex}}}{T_{\text{imp}}} = \frac{\Delta U}{R C} = \frac{M}{A}. \quad (22)$$

We use the ratio $T_{\text{ex}}/T_{\text{imp}} = M/A$ to differentiate between Phase 2 and Phase 3 of the liner implosion. When $T_{\text{ex}}/T_{\text{imp}} \ll 1$, the liner is moving at a sufficient slow velocity allowing sound waves to easily traverse the width of the liner. In this regime, the isentropic state established by the shock in Phase 1 can be maintained in flight. Hence, we designate Phase 2 as “Isentropic acceleration”. In contrast, when $T_{\text{ex}}/T_{\text{imp}} \gg 1$, sound waves traveling within the liner do not have sufficient time to fully traverse the shell width. As further elaborated in Sec. III C, the shell thickness remains approximately constant in this regime.²⁰ Therefore, we refer to Phase 3 as “Acceleration at constant shell thickness.” We shall now turn our attention to the dynamics occurring in Phase 2.

Since $M \simeq 0$ at $t = 0$, $T_{\text{ex}}/T_{\text{imp}} \simeq 0$ so the isentropic state is maintained. In this phase, the liner pressure, density, thickness, and the IFAR vary with the implosion radius R as

$$\frac{P}{P_{\text{sb}}} = \left(\frac{R}{R_0} \right)^{-2}, \quad (23a)$$

$$\frac{D}{D_{\text{sb}}} = \left(\frac{R}{R_0} \right)^{-2/\gamma}, \quad (23b)$$

$$\frac{\Delta}{\Delta_{\text{sb}}} = \left(\frac{R}{R_0} \right)^{-1+2/\gamma}, \quad (23c)$$

$$\frac{A}{A_{\text{sb}}} = \left(\frac{R}{R_0} \right)^{2-2/\gamma}. \quad (23d)$$

As shown by Eqs. (23), the liner pressure P increases with smaller radius due to the increased magnetic pressure. From Eq. (23b), the shell density increases to maintain the shell adiabat. For $\gamma = 5/3$, the liner thickness evolves as $\Delta \propto R^{1/5}$, a rather weak scaling with the liner radius. This occurs due to the compensating effects of radial convergence (increases Δ) and magnetic compression (reduces Δ). For $\gamma = 5/3$, the IFAR follows $A \propto R^{4/5}$; i.e., it decreases almost linearly with R .

Let us calculate the Mach number. When substituting

Eqs. (4), (5), (19), and (23) into Eq. (17), we obtain

$$\begin{aligned}
M^2 &= \frac{1}{\gamma P_{\text{sb}}/D_{\text{sb}}} \frac{U^2}{(P/P_{\text{sb}})/(D/D_{\text{sb}})} \\
&= \frac{\pi(R_0/\Delta T)^2}{\gamma P_{\text{sb}}/D_{\text{sb}}} \left(\frac{R}{R_0}\right)^{2-2/\gamma} \ln\left(\frac{R_0}{R}\right) \\
&= \frac{2}{\gamma-1} A_{\text{sb}} \left(\frac{R}{R_0}\right)^{2-2/\gamma} \ln\left(\frac{R_0}{R}\right) \\
&= \frac{\gamma}{(\gamma-1)^2} A_{\text{sb}} \left(\frac{A}{A_{\text{sb}}}\right) \ln\left(\frac{A_{\text{sb}}}{A}\right), \quad (24)
\end{aligned}$$

where we wrote the Mach number in terms of the IFAR using Eq. (23d) in the last line.

In Fig. 3, we plot the liner trajectory during this phase of the implosion. As the IFAR decreases, the Mach number reaches a maximum. From Eq. (24), this occurs when $A = A_{\text{max}} \doteq A_{\text{sb}}/e$, which is independent of the implosion trajectory or EOS properties. As a result, the maximum Mach number is given by

$$M_{\text{max}} = \frac{\sqrt{\gamma A_{\text{sb}}}}{(\gamma-1)} e^{-1/2}. \quad (25)$$

Interestingly, the maximum liner Mach number scales with the square root of A_{sb} as in spherical implosions.²⁰ From Eq. (23d), the radius at which the maximum Mach number occurs is given by

$$R_{\text{max}} \simeq R_0 \exp\left(-\frac{\gamma}{2\gamma-2}\right). \quad (26)$$

For $\gamma = 5/3$, we find $R_{\text{max}}/R_0 \simeq 0.29$; i.e., the liner converges by roughly a factor 3 to reach M_{max} .

Regarding the ratio of the expansion time to the implosion time, we obtain the following expression:

$$\frac{T_{\text{ex}}}{T_{\text{imp}}} = \frac{1}{\gamma-1} \sqrt{\frac{\gamma}{A_{\text{sb}}}} \left(\frac{A_{\text{sb}}}{A}\right)^{1/2} \ln^{1/2}\left(\frac{A_{\text{sb}}}{A}\right). \quad (27)$$

As the liner radially implodes, the in-flight aspect ratio decreases, and the $T_{\text{ex}}/T_{\text{imp}}$ ratio increases. Let A_\star be the IFAR value at which the implosion time T_{imp} becomes comparable to the expansion time T_{ex} , i.e., when $T_{\text{ex}} = T_{\text{imp}}$. Solving for A_\star in Eq. (27) leads to

$$\frac{A_\star}{A_{\text{sb}}} = \frac{1}{\phi_\star} W_0(\phi_\star). \quad (28)$$

Here $W_0(x)$ is the principal branch of the Lambert W -function, which is defined as the solution of the transcendental equation $W(x)e^{W(x)} = x$.⁴⁶ We also introduced the parameter ϕ_\star given by

$$\phi_\star \doteq \frac{(\gamma-1)^2}{\gamma} A_{\text{sb}}. \quad (29)$$

In the high-aspect-ratio limit ($A_{\text{sb}} \gg 1$), $W_0(\phi_\star)$ has the following asymptotic dependency:

$$W_0(\phi_\star) \simeq \ln \phi_\star - \ln \ln \phi_\star + \frac{\ln \ln \phi_\star}{\ln \phi_\star}. \quad (30)$$

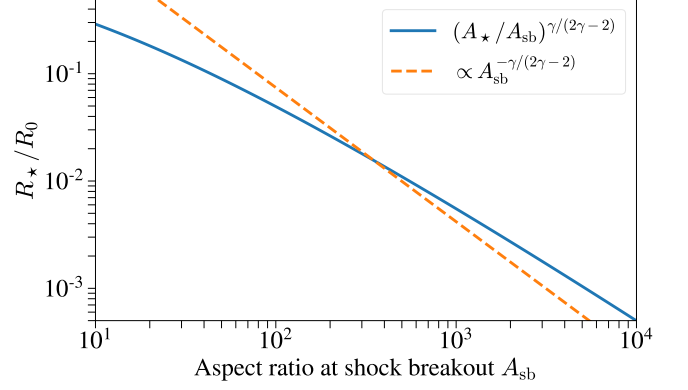


FIG. 4. Normalized liner radius R_\star/R_0 as a function of A_{sb} for the $\gamma = 5/3$ case using Eqs. (23d) and (28). The solid blue line represents R_\star given in terms of the Lambert W -function W_0 , and the dashed orange line represents the asymptotic expression of $R_\star/R_0 \propto A_{\text{sb}}^{-\gamma/(2\gamma-2)}$ of the solution.

In this limit, the dependency of A_\star on A_{sb} is only logarithmic to leading order. As an example, when considering $\gamma = 5/3$ and varying A_{sb} between 10 and 1000 in Eq. (28), we obtain $A_\star \simeq 3.7$ and $A_\star \simeq 15.6$, respectively.

To conclude this section, it is worth noting that the transition $T_{\text{ex}} = T_{\text{imp}}$ occurs relatively late in a Z-pinch implosion. Upon substituting Eq. (23d) into Eq. (28), we can calculate the radius R_\star . As observed in Fig. 4, $T_{\text{ex}} = T_{\text{imp}}$ happens almost near the point of stagnation since $R_\star/R_0 \ll 1$. For example, for $A_{\text{sb}} = 100$ and $\gamma = 5/3$, we obtain $R_\star/R_0 \simeq 0.05$; i.e., the transition occurs at a convergence ratio of approximately 20. The occurrence of the transition $T_{\text{ex}} = T_{\text{imp}}$ at a relatively late stage during a Z-pinch implosion contrasts with spherical implosions, in which this transition takes place at an earlier stage. This point will be further discussed in Sec. VIA.

C. Phase 3: Acceleration at constant shell thickness

In the next phase of the shell in-flight dynamics, $T_{\text{ex}} \gg T_{\text{imp}}$. In this regime, the shell is moving at a considerable velocity not allowing sound waves to completely traverse the width of the shell. As shown in Appendix A, the shell thickness Δ remains approximately constant during this phase of the implosion.²⁰ Hence, the liner pressure, density, thickness, and the IFAR approximately obey

$$\frac{P}{P_\star} = \left(\frac{R}{R_\star}\right)^{-\gamma}, \quad (31a)$$

$$\frac{D}{D_\star} = \left(\frac{R}{R_\star}\right)^{-1}, \quad (31b)$$

$$\Delta = \Delta_\star, \quad (31c)$$

$$\frac{A}{A_\star} = \frac{R}{R_\star}, \quad (31d)$$

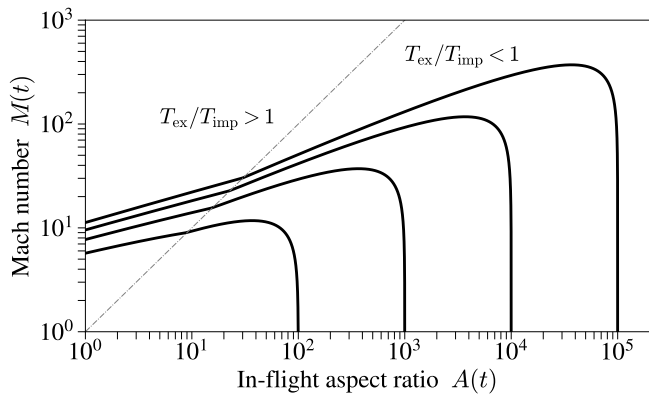


FIG. 5. Implosion trajectories in the (A, M) space for different A_{sb} values. We consider $\gamma = 5/3$.

where the “ \star ” subscript denotes quantities evaluated at $T_{ex}/T_{imp} = 1$ using Eqs. (23). Due to mass conservation, the density of the shell is inversely proportional to the shell radius meaning that the shell density rapidly increases during this phase of the implosion. To maintain the in-flight adiabat, the pressure must behave as $P \propto D^\gamma$ leading to Eq. (31a). Because $\Delta = \text{const.}$, the liner IFAR is proportional to the liner radius.

Concerning the Mach number, we find

$$\begin{aligned} \frac{M^2}{M_\star^2} &= \frac{U^2/U_\star^2}{(P/P_\star)^{1-1/\gamma}} = \frac{\ln(R_0/R)}{\ln(R_0/R_\star)} \left(\frac{R}{R_\star} \right)^{\gamma-1} \\ &= \left[1 - \frac{\ln(R/R_\star)}{\ln(R_0/R_\star)} \right] \left(\frac{R}{R_\star} \right)^{\gamma-1} \\ &= \left[1 - \frac{\ln(A/A_\star)}{\ln(R_0/R_\star)} \right] \left(\frac{A}{A_\star} \right)^{\gamma-1}. \end{aligned} \quad (32)$$

An example trajectory of the Mach number as a function of the IFAR is shown in Fig. 3 (orange line). As the shell IFAR decreases, the Mach number also decreases. However, the rate of decrease is smaller than that computed using Eq. (24). (For comparison, see the blue-dashed line in Fig. 3.)

D. Phase 4: Void closure

The “void closure” phase concerns the moment before the liner bounces off axis and the stagnation shock is launched within the liner material. Here the aspect ratio of the liner is nearly unity so that $A \simeq 1$. Hence, the radius R_{vc} of the liner at void closure is well approximated by $R_{vc} \simeq \Delta_{vc} = \Delta_\star$, where we used Eq. (31c). Since the hydrodynamic relations in Eqs. (31) depend on the ratio R/R_\star , we obtain $R_{vc}/R_\star \simeq \Delta_\star/R_\star = 1/A_\star$ at the moment of void closure. In other words, the shell hydrodynamic quantities at void closure only depend on the shell IFAR evaluated at the transition when $T_{ex} = T_{imp}$!

When using Eqs. (31), we obtain

$$P_{vc} = P_\star A_\star^\gamma, \quad (33a)$$

$$D_{vc} = D_\star A_\star, \quad (33b)$$

$$\Delta_{vc} = \Delta_\star, \quad (33c)$$

$$A_{vc} = 1, \quad (33d)$$

where the subscript “vc” denotes quantities evaluated at the moment of void closure.

Figure 5 illustrates several implosion trajectories in the (A, M) plane, where the shell aspect ratio A_{sb} at shock breakout is varied. After the initial acceleration phase, the implosion Mach number M is much greater than unity for the majority of the implosion duration. As shown, the maximum Mach number increases as the square root of A_{sb} . After the maximum Mach number has been achieved, the examples shown follow similar implosion trajectories. Finally, $M(A = 1)$ only varies by a few units even when changing the initial aspect ratio by several orders of magnitude. A similar effect occurs in spherical implosions (cf. Figure 1 of Ref. 20).

IV. SCALING LAWS FOR STAGNATION CONDITIONS WITH TARGET-DESIGN PARAMETERS

Once the shell has collided onto itself on axis, it is reasonable to assume that the internal energy of the plasma column will scale as the kinetic energy of the shell at the time of stagnation. Therefore, we have

$$\hat{\mathcal{E}}_{\text{int}} \sim \hat{m} U_{\text{stag}}^2 \sim \hat{m} \left(\frac{R_0}{\Delta T} \right)^2 \ln \left(\frac{R_0}{R_{\text{stag}}} \right), \quad (34)$$

where $\hat{\mathcal{E}}_{\text{int}}$ is the internal energy per-unit-length of the plasma column. Based on the discussion in Sec. III D, the stagnation radius R_{stag} follows $R_{\text{stag}} \simeq \Delta_\star$. The shell thickness at stagnation follows the scaling

$$\Delta_\star = R_0 \frac{R_\star}{R_0} \frac{\Delta_\star}{R_\star} = R_0 \left(\frac{A_\star}{A_{sb}} \right)^{5/4} \frac{1}{A_\star} \sim \frac{R_0}{A_{sb}^{5/4}}, \quad (35)$$

where we used Eq. (23d). In the last relation, we used the results given in Eqs. (28)–(30), which show that A_\star is a weak function of the liner aspect ratio at shock breakout. For the sake of simplicity, here and in the upcoming calculations, we shall focus on the $\gamma = 5/3$ case. Equation (35) shows that the stagnation radius scales proportionally to the initial radius of the Z pinch and is closely inverse proportional to the aspect ratio A_{sb} at shock breakout. When using Eqs. (19), we note that A_{sb} scales as

$$A_{sb} \sim \frac{R_0^{4/5} V_i^{6/5}}{\hat{m}^{2/5} \alpha_{\text{ref}}^{3/5}}, \quad (36)$$

where $V_i \doteq R_0/\Delta T$ is the characteristic implosion velocity defined in Eq. (11). When substituting Eq. (36) into

$R_{\text{stag}} \simeq R_{\text{vc}} \sim R_0 A_{\text{sb}}^{-5/4}$, we find that the pinch radius R_{stag} at stagnation scales as

$$R_{\text{stag}} \sim \frac{\alpha_{\text{ref}}^{3/4} \hat{m}^{1/2}}{V_i^{3/2}}. \quad (37)$$

Hence, to obtain more compact stagnation columns, it is necessary to increase the implosion velocity, lower the in-flight entropy parameter, and implode less massive shells.

When substituting Eq. (37) into Eq. (34), we find that the scaling of the internal energy per-unit-length of the plasma column approximately obeys

$$\hat{\mathcal{E}}_{\text{int}} \sim \hat{m} V_i^2 \ln \left(A_{\text{sb}}^{5/4} \right) \sim I_{\text{max}}^2 \ln \left(\frac{R_0 V_i^{3/2}}{\hat{m}^{1/2} \alpha_{\text{ref}}^{3/4}} \right), \quad (38)$$

where we substituted Eq. (11). Unsurprisingly, we find that $\hat{\mathcal{E}}_{\text{int}}$ primarily scales with the peak current squared applied to the Z pinch. Equation 38 also suggests that more energy can be delivered to Z pinches with higher aspect ratios. However, the dependency on the aspect ratio A_{sb} is only logarithmic. Although it is important to be aware of the logarithmic dependency on A_{sb} , we shall ignore this contribution in the ensuing calculations.

It is worth mentioning that the exact constant of proportionality between the internal energy of the plasma column and the kinetic energy of the shell prior to void closure in Eq. (38) is likely a complicated function of the shell adiabat and the spatial distribution of mass and energy within the shell. Furthermore, other non-ideal effects, such as the additional compression of the column by the magnetic field following void closure and energy leakage due to radiation losses in strongly radiating Z-pinches, will influence the scaling of the internal energy of the plasma column. Calculating the corrections associated with the aforementioned effects is beyond the scope of this paper.

To obtain the scaling of the plasma pressure at stagnation, we assume that the thermalization of the shell kinetic energy occurs at a radius R_{stag} . Therefore,

$$P_{\text{stag}} \sim \frac{\hat{\mathcal{E}}_{\text{int}}}{R_{\text{stag}}^2} \sim \frac{V_i^5}{\alpha_{\text{ref}}^{3/2}}, \quad (39)$$

where we used Eq. (37). From Eq. (39), it follows that higher stagnation pressures can be achieved by mainly increasing the implosion velocity or by decreasing the entropy parameter α_{ref} . According to this estimate, the shell mass per-unit-length does not contribute to the scaling in pressure.

Based on mass conservation, the density of the plasma column at stagnation should obey $D_{\text{stag}} R_{\text{stag}}^2 \sim \hat{m}$. Upon substitution of Eq. (37), we obtain

$$D_{\text{stag}} \sim \frac{\hat{m}}{R_{\text{stag}}^2} \sim \frac{V_i^3}{\alpha_{\text{ref}}^{3/2}}. \quad (40)$$

Hence, the shell density scales as V_i^3 with the implosion velocity and as $\alpha_{\text{ref}}^{-3/2}$ with the shell entropy parameter.

As for the pressure at stagnation, the plasma density does not show any dependency with the liner mass per-unit-length (within the accuracy of this model).

Regarding the characteristic temperature of the shell near stagnation, we pose that the temperature follows the scaling corresponding to an ideal gas such that

$$T_{\text{stag}} \sim \frac{P_{\text{stag}}}{D_{\text{stag}}} \sim V_i^2. \quad (41)$$

In other words, the temperature scales with the implosion velocity squared. It is interesting to note that, within this model, the stagnation temperature has no dependency on the shell in-flight entropy parameter.

Other important metrics for Z-pinch x-ray and neutron sources are the areal density σ_{stag} and the confinement time τ at stagnation. We expect that the areal density will obey the scaling

$$\sigma_{\text{stag}} \sim D_{\text{stag}} R_{\text{stag}} \sim \frac{\hat{m}^{1/2} V_i^{3/2}}{\alpha_{\text{ref}}^{3/4}}. \quad (42)$$

We propose that the confinement time scales as the characteristic radius of the stagnated plasma column divided by the characteristic implosion velocity. This gives

$$\tau_{\text{stag}} \sim \frac{R_{\text{stag}}}{V_i} \sim \frac{\alpha_{\text{ref}}^{3/4} \hat{m}^{1/2}}{V_i^{5/2}}. \quad (43)$$

The scaling laws derived in Eqs. (37)–(43) suggest that the implosion velocity is the most important lever for enhancing the HED conditions of the Z-pinch plasma at stagnation. We note that the V_i^5 dependency of the plasma pressure in Eq. (39) represents a stronger scaling in velocity than that for spherical laser-driven implosions, where the scaling is $P_{\text{stag}} \sim V_i^4$ (see Ref. 20). The next most important parameter is the shell entropy parameter α_{ref} . When lowered, it can increase the density, pressure, and areal density of the stagnated plasma column. Finally, increasing the mass per-unit-length \hat{m} is a useful design tool for increasing the pinch radius at stagnation, the areal density, and the confinement time.

V. SCALING LAWS FOR PERFORMANCE METRICS

A. X-ray emission by Bremsstrahlung

One application of Z pinches, such as wire arrays^{8,9} and gas puffs¹⁰, is the generation of x rays. Free-free electron bremsstrahlung emission is the dominant mechanism for soft x-ray emission for strongly ionized, low atomic number plasmas. If the stagnated plasma column is optically thin, the soft x-ray energy emission per-unit-length of a hot, uniform, cylindrical plasma is⁴⁷

$$\hat{\mathcal{P}}_{\text{ff}} \doteq \theta_{\text{ff}} \sqrt{\frac{k_{\text{B}} T_{\text{stag}}}{m_e c^2}} \frac{Z^3 D_{\text{stag}}^2}{m_i^2} \pi R_{\text{stag}}^2 \tau_{\text{stag}}, \quad (44)$$

where

$$\theta_{\text{ff}} \doteq \frac{32}{3\sqrt{6\pi}} \bar{g} \frac{\alpha^3 \hbar^2 c}{m_e}. \quad (45)$$

In the above, m_e is the electron mass, m_i is the mass of the ion species composing the Z-pinch liner, Z is the average ion charge, \bar{g} is the Gaunt factor (typically of order unity), k_B is Boltzmann's constant, $\hbar \doteq h/(2\pi)$ is the Planck constant, c is the speed of light, and $\alpha \simeq 1/137$ is the fine-structure constant. The factor πR_{stag}^2 denotes the cross-sectional area of the plasma column. When substituting the results from Sec. IV into Eq. (44), we find

$$\hat{\mathcal{P}}_{\text{ff}} \sim D_{\text{stag}}^2 T_{\text{stag}}^{1/2} R_{\text{stag}}^2 \tau_{\text{stag}} \sim \frac{\hat{m}^{3/2} V_i^{3/2}}{\alpha_{\text{ref}}^{3/4}}. \quad (46)$$

Based on Eq. (11), the product $\hat{m} V_i^2$ is constant when keeping the peak current I_{max} fixed. In this case, the x-ray energy emission by Bremsstrahlung follows

$$\hat{\mathcal{P}}_{\text{ff}} \sim \left(\frac{\hat{m}}{\alpha_{\text{ref}}} \right)^{3/4} \quad (47)$$

for $I_{\text{max}} = \text{const.}$, which shows that x-ray emission increases with the mass per-unit-length. In this vein, M. Gersten *et al.* reported experiments of imploding Al wire arrays in which the radius and mass per-unit-length were scaled to approximately satisfy $\hat{m} R_0^2 = \text{const.}$ ⁴⁸ In those experiments, the smaller-radius, larger-mass targets led to lower-temperature and higher-density stagnated plasma columns. (In accordance to the scaling laws for the stagnation conditions presented in Sec. IV.) In particular, the ~ 5 x more massive implosion produced ~ 30 x more x-ray yield (above 1 keV) than the control target with nominal mass per-unit-length. When using Eq. (47), we find an expected increase of only 3x. It is reassuring that Eq. (47) qualitatively reproduces the observed trend in performance; however, the observed increase in performance in the experiments is much higher than what theory suggests. Possible reasons for the discrepancy are that the larger-in-radius (less massive) targets are more prone to in-flight instabilities, have higher kinetic energy per nuclei at stagnation, and could be more susceptible to turbulence heating.⁷ These non-ideal effects could result in larger, higher-temperature, lower-density plasma columns with lower emissivity at stagnation.

B. X-ray emission by bound-bound transitions

In a fully ionized plasma, x rays are emitted in a continuous spectrum, reflecting the fact that the emitted photons originate from free electrons which begin in one plane-wave state and end in a different plane-wave state as a result of the emission. By contrast, a plasma in which the ionization is incomplete harbors atoms with

electrons that remain in various bound states. Transitions between two of these discrete states results in emission lines characteristic of the radiating element. Many Z-pinch implosions are geared toward generating conditions under which copious amounts of He- α x rays are produced (that is, x rays engendered by transitions from the atomic L shell to the K shell in atoms ionized down to the final two electrons). This is the dominant form of soft x-ray emission in partially ionized mid-atomic number plasmas. The emitted energy per-unit-length resulting from bound-bound transitions from principal quantum number $m \rightarrow n$ in a cylindrical stagnation column is given by⁴⁹

$$\hat{\mathcal{P}}_{\text{bb}} = \theta_{\text{bb}} \sqrt{\frac{m_e c^2}{k_B T_{\text{stag}}}} \exp\left(\frac{-E_{mn}}{k_B T_{\text{stag}}}\right) \frac{Z D_{\text{stag}}^2}{m_i^2} \pi R_{\text{stag}}^2 \tau_{\text{stag}}, \quad (48)$$

where

$$\theta_{\text{bb}} \doteq 8\pi \sqrt{\frac{\pi}{6}} \bar{g} f_{mn} \frac{\alpha^2 \hbar^2 c}{m_e}, \quad (49)$$

E_{mn} is the energy of the emitted photon, and f_{mn} is the oscillator strength of the transition.

The temperature dependence of Eq. (48) can be simplified by imposing a power law form and solving for the power index that satisfies the imposed identity. That is, we seek the n that satisfies

$$\frac{\hat{\mathcal{P}}_{\text{bb}}(T)}{\hat{\mathcal{P}}_{\text{bb}}(T_0)} \simeq \left(\frac{T}{T_0}\right)^n, \quad (50)$$

for temperatures in the vicinity of some desired T_0 .

To isolate the temperature dependence of Eq. (48), we group the temperature-independent factors into a constant b and define $\delta \doteq E_{mn}/k_B$ so that Eq. (48) becomes

$$\hat{\mathcal{P}}_{\text{bb}}(T) = \frac{b}{\sqrt{T}} e^{-\delta/T}. \quad (51)$$

Solving for n in Eqs. (50) and (51) yields

$$n = \frac{\ln\left(\frac{\hat{\mathcal{P}}_{\text{bb}}(T)}{\hat{\mathcal{P}}_{\text{bb}}(T_0)}\right)}{\ln\left(\frac{T}{T_0}\right)} = \frac{\frac{\delta}{T} \left[\frac{T}{T_0} - 1\right]}{\ln\left(\frac{T}{T_0}\right)} - \frac{1}{2}, \quad (52)$$

The first term of the Taylor expansion of $\ln(T/T_0)$ is $(T/T_0 - 1)$. Therefore, the power index itself is a function of temperature and equal (in first order) to

$$n = \frac{\delta}{T} - \frac{1}{2}. \quad (53)$$

Note that this scaling is only approximate in the sense that any calculation of the x-ray yield increase resulting from an increase in temperature necessarily spans multiple temperatures, all with different power indices. When calculating the scaling at a given temperature T_0 , however, Eq. (53) is exact. This is because $\ln x \simeq (x - 1)$

when $x \simeq 1$, so keeping only the first term in the Taylor expansion yields no error, and the slope of the “true” function (51) exactly matches that of T^n . The region around T_0 over which this scaling is valid depends ultimately on how quickly the other terms in the expansion begin to contribute, which generally manifests in relatively small windows for $T \ll \delta$, and large windows when $T \simeq \delta$. The emission is roughly constant when the plasma temperature is comparable to the energy of the line of interest, as can be observed from Eq. (53), resulting in a large temperature range over which Eq. (53) applies. For example, in a 1.85 keV neon plasma—whose He- α line is 0.922 keV—the emission is constant with respect to temperature for $1.08 \text{ keV} \leq T \leq 4.35 \text{ keV}$, while a krypton plasma (He- α line of 13.114 keV) of equal temperature has $\hat{P}_{\text{bb}} \propto T^{6.6}$ for $1.57 \text{ keV} \leq T \leq 2.22 \text{ keV}$, where the bounds indicate the region over which the approximate function is within 10% of the exact value.

The preceding discussion makes clear that the scaling of bound-bound emission with temperature depends intimately on which lines are being pursued and which temperature ranges are accessible with the Z-pinch. In reality, a wide range of plasma parameters can be realized depending on the specific scheme being employed, so in order to ultimately find a proper current scaling we must apply constraints that do not pertain to all Z-pinches. As an exemplary plasma, we consider only the 3.14 keV He- α line of argon at $T_{\text{stag}} = 1.85 \text{ keV}$,⁵⁰ yielding $\hat{P}_{\text{bb}} \propto D_{\text{stag}}^2 T_{\text{stag}}^{1.2} R_{\text{stag}}^2 \tau_{\text{stag}}$. We can use the results from Sec. IV to conclude

$$\hat{P}_{\text{bb}} \sim \frac{\hat{m}^{3/2}}{\alpha_{\text{ref}}^{3/4}} V_i^{2.9}. \quad (54)$$

Despite having a rather distinct origin from the bremsstrahlung x-ray production, x-ray line emission shares a similar scaling relationship with respect to the mass per-unit-length and the entropy parameter. However, the dependency on the shell velocity is stronger for line emission as compared to bremsstrahlung emission.

C. Neutron yield

Another studied application of Z pinches is the production of neutrons via nuclear fusion. One widely studied Z-pinch neutron source is the gas puff.^{11,12} For a Z pinch liner composed of equimolar DT fuel, the neutron yield per-unit-length is approximately given by⁴⁷

$$\hat{Y} = \frac{1}{4} \left(\frac{D_{\text{stag}}}{m_i} \right)^2 \langle \sigma v \rangle_{\text{DT}} \pi R_{\text{stag}}^2 \tau_{\text{stag}}, \quad (55)$$

where $\langle \sigma v \rangle_{\text{DT}}$ is the DT fusion reactivity. Between the 3- and 5-keV temperature range, the DT fusion reactivity can be approximated by $\langle \sigma v \rangle_{\text{DT}} \sim T^4$.^{51,52} When substituting the results from Sec. IV into Eq. (55), we find

$$\hat{Y} \sim D_{\text{stag}}^2 T_{\text{stag}}^4 R_{\text{stag}}^2 \tau \sim \frac{\hat{m}^{3/2} V_i^{17/2}}{\alpha_{\text{ref}}^{3/4}}. \quad (56)$$

In this case, due to the strong dependency with the ion temperature at stagnation, the neutron yield scales strongly with the characteristic implosion velocity V_i .

It is interesting to note that, for both x-ray emission and neutron yield, there is a stronger dependency on the liner mass per-unit-length \hat{m} as compared to the shell entropy parameter α_{ref} . In other words, the shell entropy parameter α_{ref} seems to play a more prominent role in the determination of the plasma conditions at stagnation, but the mass per-unit-length becomes a more important parameter when considering integrated performance of a Z-pinch x-ray or neutron source.

VI. DISCUSSION

A. Comparison of the in-flight dynamics for cylindrical Z-pinch implosions and spherical laser-driven implosions

Let us now compare and contrast the in-flight dynamics of cylindrical Z-pinch implosions and spherical laser-driven implosions. Regarding the latter, a common approximation is to consider the external pressure drive as constant in time. Then, the momentum-conservation equation for a high-aspect-ratio spherical shell is

$$m_{\text{shell}} \frac{d^2 R}{dt^2} = -4\pi R^2 P_{\text{sb}}, \quad (57)$$

where m_{shell} is the mass of the shell and P_{sb} is the pressure drive after shock breakout. Integrating the equation above gives the energy equation:

$$\left(\frac{dR}{dt} \right)^2 = \frac{8\pi P_{\text{sb}}}{3m_{\text{shell}}} (R_0^3 - R^3), \quad (58)$$

which we shall use to calculate the shell Mach number.

During the isentropic-acceleration phase of a spherical implosion, the shell pressure, density, thickness, and IFAR obey²⁰

$$\begin{aligned} \frac{P}{P_{\text{sb}}} &= 1, & \frac{D}{D_{\text{sb}}} &= 1, \\ \frac{\Delta}{\Delta_{\text{sb}}} &= \left(\frac{R}{R_0} \right)^{-2}, & \frac{A}{A_{\text{sb}}} &= \left(\frac{R}{R_0} \right)^3. \end{aligned} \quad (59)$$

The in-flight Mach number is given by

$$M^2 = \frac{U^2}{\gamma P_{\text{sb}}/D_{\text{sb}}} = \frac{2A_{\text{sb}}}{3(\gamma - 1)} \left(1 - \frac{A}{A_{\text{sb}}} \right), \quad (60)$$

where we used $m_{\text{shell}} \simeq 4\pi\rho_0 R_0^2 \Delta_0$ and substituted Eqs. (19b)–(19d), (58), and (59).

Let us now compare Eqs. (59) and (60) for a spherical implosion to the results found in Eqs. (23) and (24) for a Z-pinch implosion. Due to the constant pressure drive and conservation of the shell adiabat, the shell pressure and density do not change in the spherical case. In contrast, the liner density for a Z-pinch increases as the

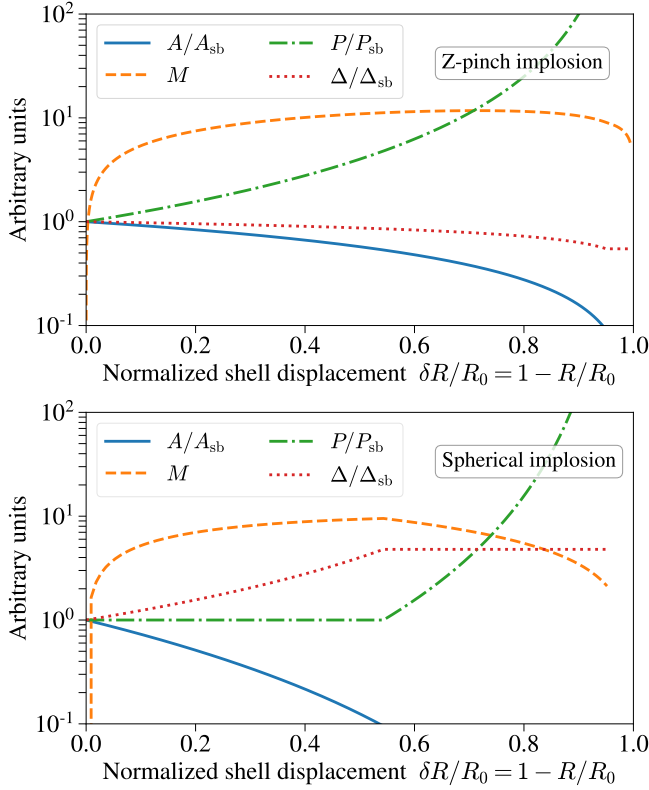


FIG. 6. Evolution of the normalized aspect ratio A/A_{sb} , Mach number M , normalized pressure P/P_{sb} , and normalized shell thickness Δ/Δ_{sb} for a Z-pinch implosion (top) and a spherical implosion (bottom). For both cases, we consider $A_{sb} = 10^2$ and $\gamma = 5/3$.

implosion proceeds. This represents an advantage for Z pinches since this effect is beneficial for increasing the in-flight ram pressure of the shell. The evolution of the shell pressure is illustrated in the green dot-dashed curves in Fig. 6 for both cases. For this comparison, we set the initial aspect ratio at shock breakout to be equal for both cases. It is worth mentioning that, for the spherical case, the shell thickness increases as R^{-2} , and the shell IFAR decreases as R^3 . These trends are advantageous for spherical implosions compared to Z-pinch since the expansion of the shell width and the subsequent faster decrease in IFAR are beneficial for mitigating the feedthrough of the Rayleigh–Taylor instability. The evolution of the shell thickness and the IFAR are illustrated by the solid blue lines and red dotted lines in Fig. 6, respectively.

After the isentropic-acceleration phase, an imploding spherical shell reaches the “coasting” phase, where $T_{ex} > T_{imp}$ and the shell thickness remains approximately constant. Here the pressure, density, thickness, IFAR,

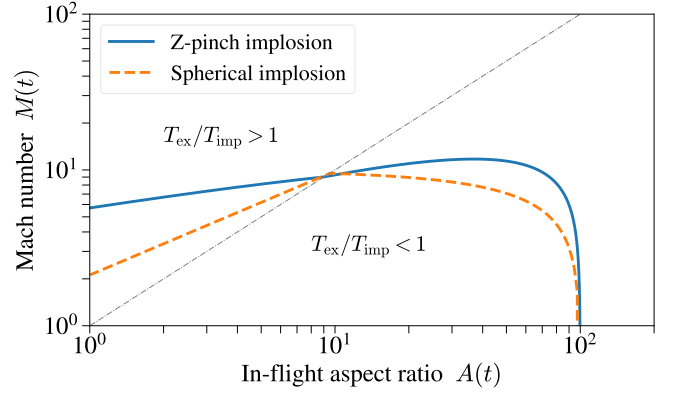


FIG. 7. Implosion trajectories in the (A, M) space for a magnetically-driven cylindrical Z pinch and a laser-driven spherical implosion. For both cases, we consider $A_{sb} = 10^2$ and $\gamma = 5/3$.

and Mach number obey²⁰

$$\begin{aligned} \frac{P}{P_\star} &= \left(\frac{R}{R_\star}\right)^{-2\gamma}, & \frac{D}{D_\star} &= \left(\frac{R}{R_\star}\right)^{-2}, & \Delta &= \Delta_\star, \\ \frac{A}{A_\star} &= \left(\frac{R}{R_\star}\right), & \frac{M}{M_\star} &\simeq \left(\frac{R}{R_\star}\right)^{\gamma-1}. \end{aligned} \quad (61)$$

During this stage, the shell density amplifies as R^{-2} due to spherical-convergence effects. This leads to large amplification of the in-flight ram pressure and high pressures at stagnation. The sudden jump in the shell pressure is observed in Fig. 6 (bottom).

An important difference shown in Fig. 6 is that, for spherical implosions, the implosion-at-constant-thickness phase occurs relatively early when $R_\star/R_0 \simeq 0.45$ for the example given in Fig. 6. For Z-pinch implosions, this stage begins when $R_\star/R_0 \simeq 0.05$, meaning that the transition $T_{ex} > T_{imp}$ occurs right before the moment of stagnation (see Fig. 4). This noticeable difference between the two imploding systems can be explained by the magnetic-drive of Z pinches, where the ever increasing magnetic pressure increases the characteristic sound-propagation speed inside the shell and delays the transition to the constant-thickness phase.

To conclude this section, in Fig. 7, we compare the implosion trajectories in the (A, M) parametric plane for a cylindrical Z-pinch and a spherical laser-driven shell. Regarding the Mach number M , the Z-pinch case reaches a maximum during the acceleration phase but subsequently decreases as the IFAR decreases. Conversely, the Mach number for spherical implosions increases as the IFAR decreases when $T_{ex}/T_{im} < 1$. In Fig. 7, the transition $T_{ex}/T_{im} = 1$ occurs at $A_\star \simeq 9$ for both cases. However, it is important to note that this observation pertains specifically to the example utilizing $A_{sb} = 100$ and $\gamma = 5/3$ and should not be considered as a general property. When $T_{ex}/T_{im} > 1$, the spherical implosion case exhibits a more pronounced decrease in the Mach

number. This phenomenon arises because, in spherical implosions, once the radius of the shell diminishes sufficiently, the acceleration of the shell becomes negligible. Consequently, the shell velocity remains relatively constant, while the shell pressure and density increase significantly during the coasting phase. In contrast, the Z-pinch continues to be accelerated due to the increasing magnetic pressure drive, which partially offsets the rising shell density and pressure during the latter stages of the implosion. Despite the differences in the implosion trajectories in the (A, M) plane for spherical and Z-pinch imploding systems, our estimates indicate that both systems converge to final Mach number values greater than unity at stagnation when starting with the same in-flight aspect ratios. Therefore, we conclude that the stagnation pressure of a spherical or Z-pinch implosion is a result of an amplification of the in-flight hydrodynamic (or ram) pressure prior to void closure, not of the pressure source driving the implosion.

B. Similarity scaling Z-pinch implosions with respect to peak current

From the results presented in Secs. IV and V, we may also determine the extrapolation scaling laws for the stagnation conditions and performance metrics when increasing the peak current driving a Z pinch. One convenient scaling strategy presented in Refs. 36, 37, 53, and 54 is to scale Z-pinch implosions so that dynamic similarity is maintained between the baseline and scaled load designs. To achieve this, one strategy is to scale the target design parameters such that the implosion time ΔT remains constant. Maintaining ΔT invariant in Eq. (5) when increasing the peak current leads to the scaling relation $\hat{m}R_0^2 \propto I_{\max}^2$. In the high-aspect-ratio limit, the scaling law above becomes

$$R_0 \propto \frac{I_{\max}^{1/2} A_0^{1/4}}{\rho_0^{1/4}} \propto I_{\max}^{1/2} A_0^{1/4}. \quad (62)$$

In what follows, we shall consider that the liner material is left unchanged when scaling up in current. Thus, the initial liner density ρ_0 is considered constant.

1. Current scaling while holding constant the initial aspect ratio A_0

When scaling with respect to peak current while keeping the implosion time constant, there are two possibilities worth considering. The first option involves increasing the liner radius while maintaining the initial liner aspect ratio A_0 constant. Such scaling strategy may be more appropriate for wire-array implosions, whose effective IFARs are higher compared to solid metallic liner implosions, such as MagLIF.^{14,55–57} Upon using Eq. (62),

we find that the initial liner radius, the mass per-unit-length, and the characteristic implosion velocity scale as

$$R_0 \propto V_i \propto I_{\max}^{1/2}, \quad \hat{m} \propto I_{\max}. \quad (63)$$

We insert Eqs. (63) into the asymptotic scaling laws found in Secs. IV and V for the stagnation conditions and performance metrics. The resulting extrapolation scaling laws are summarized in the third column of Table I. From the algebraic manipulations, the noteworthy results are the following: (i) the temperature at stagnation scales linearly with current ($T_{\text{stag}} \propto I_{\max}$), (ii) the stagnation pressure scales with current as ($P_{\text{stag}} \propto I_{\max}^{5/2}$), which is a much stronger scaling law compared to the $P_{\text{mag}} \propto I_{\max}$ scaling law for the magnetic-drive pressure, (iii) the confinement time is expected to decrease even though the implosion time ΔT is conserved ($\tau_{\text{stag}} \propto I_{\max}^{-3/4}$), (iv) the K-shell emission per-unit-length approximately scales as ($\hat{P}_{\text{bb}} \propto I_{\max}^{2.95}$), and (v) the neutron yield per-unit-length scales strongly with current ($\hat{Y} \propto I_{\max}^{5.75}$). Regarding the last point, it is interesting to note that the predicted scaling relation for the neutron yield is more optimistic than the typically quoted I_{\max}^4 scaling law in the Z-pinch literature.¹²

2. Current scaling while holding constant the aspect ratio A_{sb} at shock breakout

The scaling strategy proposed in Sec. VIB 1 keeps the initial aspect ratio of the liner constant, which then leads to an aggressive scaling of the liner initial radius. A more conservative approach designed to mitigate the effects of Rayleigh–Taylor instabilities is to scale the liner radius and mass such that the in-flight aspect ratio at shock breakout is maintained; i.e., $A_{\text{sb}} = \text{const}$. This scaling approach was proposed in Refs. 36 and 37. From Eqs. (19) and (62), we find that the liner outer radius and mass per-unit-length obey

$$\frac{R_0^4}{A_0} \propto I_{\max}^2, \quad R_0^{2/\gamma} \propto \frac{1}{A_0^{1-1/\gamma}}. \quad (64)$$

We consider a polytropic index of $\gamma = 5/3$ and obtain

$$R_0 \propto V_i \propto I_{\max}^{2/7}, \quad \hat{m} \propto I_{\max}^{10/7}. \quad (65)$$

Comparing the scaling prescriptions in Eqs. (65) to those in Eqs. (63), we find that the scaled liners grow more slowly in radius and their mass increases at a faster rate. In fact, with this scaling strategy, the liner initial aspect ratio decreases almost linearly with current: $A_0 \propto I_{\max}^{-6/7}$.

We insert the scaling prescriptions in Eqs. (65) into the asymptotic scaling laws found in Secs. IV and V for the stagnation conditions and performance metrics. The resulting extrapolation scaling laws are summarized in the fourth column of Table I. Comparing the results between the third and the fourth columns, we find that the extrapolation scaling laws using a fixed initial aspect ratio tend to be more favorable. This occurs because the

TABLE I. Asymptotic scaling laws for stagnation conditions, energetic quantities, and performance metrics of a high-aspect-ratio ($A \gg 1$) Z-pinch implosion. A polytropic index of $\gamma = 5/3$ is considered in the summarized results below.

Physical quantity	Asymptotic scaling	Current scaling at fixed initial aspect ratio A_0	Current scaling at fixed in-flight aspect ratio A_{sb}
Stagnation radius R_{stag}	$\frac{\alpha_{ref}^{3/4} \hat{m}^{1/2}}{V_i^{3/2}}$	$I_{max}^{-1/4}$	$I_{max}^{2/7}$
Stagnation density D_{stag}	$\frac{V_i^3}{\alpha_{ref}^{3/2}}$	$I_{max}^{3/2}$	$I_{max}^{6/7}$
Stagnation pressure P_{stag}	$\frac{V_i^5}{\alpha_{ref}^{3/2}}$	$I_{max}^{5/2}$	$I_{max}^{10/7}$
Stagnation temperature T_{stag}	V_i^2	I_{max}	$I_{max}^{4/7}$
Areal density σ_{stag}	$\frac{\hat{m}^{1/2} V_i^{3/2}}{\alpha_{ref}^{3/4}}$	$I_{max}^{5/4}$	$I_{max}^{8/7}$
Confinement time τ_{stag}	$\frac{\hat{m}^{1/2} \alpha_{ref}^{3/4}}{V_i^{5/2}}$	$I_{max}^{-3/4}$	const.
Internal energy per-unit-length $\hat{\mathcal{E}}_{int}$	$\hat{m} V_i^2$	I_{max}^2	I_{max}^2
Kinetic energy per-unit-length $\hat{\mathcal{E}}_{kin}$	$\hat{m} V_i^2$	I_{max}^2	I_{max}^2
Bremsstrahlung emission per-unit-length \hat{P}_{ff}	$\frac{\hat{m}^{3/2} V_i^{3/2}}{\alpha_{ref}^{3/4}}$	$I_{max}^{2.25}$	$I_{max}^{2.57}$
X-ray line emission per-unit-length \hat{P}_{bb} (at $E_{mn}/k_B T \simeq 1.7$)	$\frac{\hat{m}^{3/2} V_i^{2.9}}{\alpha_{ref}^{3/4}}$	$I_{max}^{2.95}$	$I_{max}^{2.97}$
Neutron production per-unit-length \hat{Y} (at $3 \text{ keV} \leq T \leq 5 \text{ keV}$)	$\frac{\hat{m}^{3/2} V_i^{17/2}}{\alpha_{ref}^{3/4}}$	$I_{max}^{5.75}$	$I_{max}^{4.57}$

liner velocity increases more strongly in Eqs. (63). Nevertheless, the scaling law for the neutron yield following the second scaling strategy (with fixed in-flight aspect ratio) is still more optimistic than the typical I_{max}^4 scaling law. It is surprising that the second scaling strategy shows a more favorable scaling law for the generation of x-rays compared to the first strategy. This is due to the strong dependency of x-ray emission on the mass per-unit-length, which increases more strongly in Eqs. (65).

An important observation to conclude this section is that, for both scaling strategies, the x-ray emission demonstrates a weaker dependence on peak current compared to the neutron yield. This suggests that, when enhancing the peak current and employing similarity scaling of Z-pinch configurations, increasing the x-ray emission is harder than increasing the neutron yield.

VII. CONCLUSIONS

In this work, we theoretically investigated the in-flight dynamics of a magnetically-driven, imploding cylindrical shell that stagnates onto itself upon collision on axis. The converging flow of the Z-pinch is analyzed by considering the implosion trajectory in the (A, M) parametric plane, where A is the in-flight aspect ratio and M is the implo-

sion Mach number. For an ideal implosion in the absence of instabilities, we derived the asymptotic scaling laws for hydrodynamic quantities (e.g., density, temperature, and pressure) evaluated at stagnation as functions of target-design parameters. We obtained the asymptotic scaling laws for various metrics measuring the performance of popular Z-pinch applications, including x-ray emission and neutron yield.

Our study suggests that the Z-pinch implosion velocity is the most important lever for enhancing the HED conditions of the Z-pinch plasma at stagnation. For the hydrodynamic conditions at stagnation of the Z pinch plasma (e.g., density, temperature, and pressure), the next most important parameter is the shell entropy parameter α_{ref} . When lowered, it can increase the density, pressure, and areal density of the Z pinch at stagnation. For integrated performance metrics, such as x-ray emission and neutron yield, the mass per-unit-length \hat{m} plays a more prominent role compared to the entropy parameter.

This work also compares the kinematics of cylindrical Z-pinch implosions and spherical laser-driven implosions. These systems differ in two major aspects. For Z pinches, the magnetic pressure driving the implosion increases as the shell converges on axis, leading to a *continuously* increasing shell density and pressure in flight. Our analysis suggests that the implosion phase, during which the

shell thickness remains constant, occurs relatively late in Z-pinch implosions (i.e., at high convergence ratios). Therefore, the magnetic-drive pressure in Z-pinch implosions plays an important role in establishing the final implosion velocity of the shell and the in-flight density profile. Both factors contribute to the hydrodynamic (or ram) pressure and to the final stagnation pressure.

For spherical implosions, the drive pressure is approximately constant, and the shell acceleration weakens as the surface area of the spherical shell decreases. Thus, it becomes more difficult to accelerate a spherical shell once the convergence ratio is greater than 2 or 3. Since the drive pressure is approximately constant, there are no gains in the hydrodynamic pressure due to increases in the shell density during the first phase of the implosion. However, the coasting phase, where the shell thickness remains approximately constant, occurs relatively early in spherical implosions. This phase is crucial for spherical implosions because the shell density and pressure amplify dramatically during this phase, increasing the hydrodynamic pressure and leading to high pressure at stagnation. Despite the differences in the implosion trajectories in the (A, M) parametric plane for spherical and Z-pinch imploding systems, both systems converge to similar final Mach number values at stagnation when starting with the same in-flight aspect ratios.

As a final remark, we emphasize that the scaling laws presented in this study are derived for an idealized one-dimensional Z-pinch implosion. A number of non-ideal effects are not considered in this analysis; for example, hydrodynamic instabilities, complex 2D and 3D hydrodynamic flows, finite-conductivity phenomena, and energy-loss mechanisms occurring in-flight during the implosion and at stagnation. Incorporating these effects would undoubtedly alter the scaling exponents obtained in Secs. IV and V for the stagnation conditions and performance metrics of a Z-pinch implosion.

For future research, we propose the following plan to test the scaling laws presented in this study against simulation results and experimental data. As an initial step, it would be beneficial to validate the scaling laws through 1D radiation-magneto-hydrodynamic simulations that incorporate finite-conductivity phenomena and energy-transport mechanisms. Subsequent efforts can focus on investigating the effects of hydrodynamic instabilities and complex multi-dimensional hydrodynamic flows, including the influence of residual kinetic energy on performance degradation.^{58,59} Finally, existing experimental data can be analyzed to uncover underlying scaling laws that reflect the parametric dependencies discussed in this work.

The data that support the findings of this study are available from the corresponding author upon reasonable request.

Sandia National Laboratories is a multitechnology laboratory managed and operated by National Technology & Engineering Solutions of Sandia, LLC, a wholly owned subsidiary of Honeywell International Inc., for the U.S.

Department of Energy's National Nuclear Security Administration under contract DE-NA0003525. This paper describes objective technical results and analysis. Any subjective views or opinions that might be expressed in the paper do not necessarily represent the views of the U.S. Department of Energy or the U.S. Government.

Appendix A: Constant shell thickness during Phase 3 of the implosion

The radial momentum equation with the magnetic pressure term included reads as

$$\rho \left(\frac{\partial v_r}{\partial t} + v_r \frac{\partial}{\partial r} v_r \right) = -\frac{\partial p}{\partial r} - \frac{\partial p_m}{\partial r}. \quad (\text{A1})$$

We write the radial velocity as $v_r(t, r) = \dot{R}(t) + \delta v_r(t, r)$. Upon noting that $\rho \sim \hat{m}/(2\pi R\Delta)$ and $\partial_r p_m \sim P_m/\Delta$ and using Eq. (1), we have

$$\frac{\partial}{\partial t} \delta v_r + (\dot{R} + \delta v_r) \frac{\partial}{\partial r} \delta v_r = -\frac{1}{\rho} \frac{\partial p}{\partial r}. \quad (\text{A2})$$

The correction velocity scales as $\delta v_r \sim \dot{\Delta}$. The temporal and radial derivatives scale with the implosion time and the shell thickness; that is, $\partial_t \sim T_{\text{imp}}^{-1} = R/\dot{R}$ and $\partial_r \sim \Delta^{-1}$. When noting that $p/\rho \sim P/D \sim C_s^2$, we have

$$\frac{\dot{\Delta}}{R/\dot{R}} + \frac{\dot{R}\dot{\Delta}}{\Delta} + \frac{\dot{\Delta}^2}{\Delta} \sim \frac{C_s^2}{\Delta}. \quad (\text{A3})$$

The second term dominates the third one since $\dot{\Delta} \ll \dot{R}$ for a high-aspect-ratio shell. Therefore, we obtain the following balance relation:

$$\underbrace{\frac{\dot{\Delta}}{R/\dot{R}}}_1 + \underbrace{\frac{\dot{R}\dot{\Delta}}{\Delta}}_2 \sim \underbrace{\frac{C_s^2}{\Delta}}_3. \quad (\text{A4})$$

If terms #1 and #2 dominate over #3, then $\dot{\Delta} \sim 0$; that is, the shell thickness remains constant. If term #1 is balanced by #3, we have $\dot{\Delta} \sim (C_s^2/\Delta)(R/\dot{R})$. When denoting the change in the liner thickness by $\delta\Delta \sim \dot{\Delta} T_{\text{imp}} = \dot{\Delta}(R/\dot{R})$, we obtain

$$\frac{\delta\Delta}{\Delta} \sim \frac{C_s^2 R^2}{\dot{R}^2 \Delta^2} = \frac{A^2}{M^2} \ll 1, \quad (\text{A5})$$

where $A \ll M$ since the expansion time is much longer than the implosion time during Phase 3 of the implosion [see Eq. (22)]. Finally, if term #2 is balanced by term #3, we obtain $\dot{\Delta} \sim C_s^2/\dot{R}$. Then,

$$\frac{\delta\Delta}{\Delta} \sim \frac{C_s^2 R}{\dot{R}^2 \Delta} = \frac{A}{M^2} < \frac{A}{M} \ll 1, \quad (\text{A6})$$

where we used $M > 1$. Therefore, $\delta\Delta/\Delta \ll 1$; i.e., the shell thickness remains approximately constant during Phase 3 of the implosion.

- ¹M. K. Matzen, C. Deeney, R. J. Leeper, J. L. Porter, R. B. Spielman, G. A. Chandler, M. S. Derzon, M. R. Douglas, D. L. Fehl, D. E. Hebron, et al., “Fast z-pinch as dense plasma, intense x-ray sources for plasma physics and fusion applications,” *Plasma Phys. Control. Fusion* **41**, A175 (1999).
- ²D. D. Ryutov, M. S. Derzon, and M. K. Matzen, “The physics of fast Z pinches,” *Rev. Mod. Phys.* **72**, 167 (2000).
- ³M. K. Matzen, M. A. Sweeney, R. G. Adams, J. R. Asay, J. E. Bailey, G. R. Bennett, D. E. Bliss, D. D. Bloomquist, T. A. Brunner, R. B. Campbell, et al., “Pulsed-power-driven high energy density physics and inertial confinement fusion research,” *Phys. Plasmas* **12**, 055503 (2005).
- ⁴M. G. Haines, “A review of the dense Z-pinch,” *Plasma Phys. Control. Fusion* **53**, 093001 (2011).
- ⁵R. D. McBride, W. A. Stygar, M. E. Cuneo, D. B. Sinars, M. G. Mazarakis, J. J. Leckbee, M. E. Savage, B. T. Hutsel, J. D. Douglass, M. L. Kiefer, et al., “A primer on pulsed power and linear transformer drivers for high energy density physics applications,” *IEEE Trans. Plasma Sci.* **46**, 3928 (2018).
- ⁶D. B. Sinars, M. A. Sweeney, C. S. Alexander, D. J. Ampleford, T. Ao, J. P. Apruzese, C. Aragon, D. J. Armstrong, K. N. Austin, T. J. Awe, et al., “Review of pulsed power-driven high energy density physics research on Z at Sandia,” *Phys. Plasmas* **27**, 070501 (2020).
- ⁷N. R. Pereira and J. Davis, “X rays from Z-pinch on relativistic electron-beam generators,” *J. Appl. Phys.* **64**, R1 (1988).
- ⁸M. E. Cuneo, E. M. Waisman, S. V. Lebedev, J. P. Chittenden, W. A. Stygar, G. A. Chandler, R. A. Vesey, E. P. Yu, T. J. Nash, D. E. Bliss, et al., “Characteristics and scaling of tungsten-wire-array Z-pinch implosion dynamics at 20 MA,” *Phys. Rev. E* **71**, 046406 (2005).
- ⁹J. Schwarz, R. A. Vesey, D. J. Ampleford, M. A. Schaeuble, A. L. Velikovich, J. L. Giuliani, A. Esaulov, A. Dasgupta, and B. Jones, “A model for K-shell x-ray yield from magnetic implosions at Sandia’s Z machine,” *Phys. Plasmas* **29**, 103101 (2022).
- ¹⁰J. L. Giuliani and R. J. Commisso, “A review of the gas-puff Z-pinch as an x-ray and neutron source,” *IEEE Trans. Plasma Sci.* **43**, 2385 (2015).
- ¹¹C. A. Coverdale, C. Deeney, A. L. Velikovich, R. W. Clark, Y. K. Chong, J. Davis, J. Chittenden, C. L. Ruiz, G. W. Cooper, A. J. Nelson, et al., “Neutron production and implosion characteristics of a deuterium gas-puff Z pinch,” *Physics of Plasmas* **14**, 022706 (2007).
- ¹²A. L. Velikovich, R. W. Clark, J. Davis, Y. K. Chong, C. Deeney, C. A. Coverdale, C. L. Ruiz, G. W. Cooper, A. J. Nelson, J. Franklin, et al., “Z-pinch plasma neutron sources,” *Phys. Plasmas* **14**, 022701 (2007).
- ¹³S. A. Slutz and R. A. Vesey, “High-gain magnetized inertial fusion,” *Phys. Rev. Lett.* **108**, 1139 (2012).
- ¹⁴M. R. Gomez, S. A. Slutz, A. B. Sefkow, D. B. Sinars, K. D. Hahn, S. B. Hansen, E. C. Harding, P. F. Knapp, P. F. Schmit, C. A. Jennings, et al., “Experimental demonstration of fusion-relevant conditions in magnetized liner inertial fusion,” *Phys. Rev. Lett.* **113**, 155003 (2014).
- ¹⁵M. R. Gomez, S. A. Slutz, C. A. Jennings, D. J. Ampleford, M. R. Weis, C. E. Myers, D. A. Yager-Elorriaga, K. D. Hahn, S. B. Hansen, E. C. Harding, et al., “Performance scaling in magnetized liner inertial fusion experiments,” *Phys. Rev. Lett.* **125**, 155002 (2020).
- ¹⁶J. E. Bailey, T. Nagayama, G. P. Loisel, G. A. Rochau, C. Blancard, J. Colgan, P. Cosse, G. Faussurier, C. J. Fontes, G. Gilleron, et al., “A higher-than-predicted measurement of iron opacity at solar interior temperatures,” *Nature* **517**, 56 (2015).
- ¹⁷T. Nagayama, J. Bailey, G. Loisel, G. Dunham, G. Rochau, C. Blancard, J. Colgan, P. Cossé, G. Faussurier, C. Fontes, et al., “Systematic study of L-shell opacity at stellar interior temperatures,” *Phys. Rev. Lett.* **122**, 235001 (2019).
- ¹⁸V. Valenzuela-Villaseca, L. Suttle, F. Suzuki-Vidal, J. Halliday, S. Merlini, D. Russell, E. Tubman, J. Hare, J. Chittenden, M. Koepke, et al., “Characterization of quasi-Keplerian, differentially rotating, free-boundary laboratory plasmas,” *Phys. Rev. Lett.* **130**, 195101 (2023).
- ¹⁹Finite-conductivity effects can manifest themselves as diffusion of the azimuthal magnetic field driving the Z-pinch implosion and the corresponding Ohmic heating of the Z-pinch shell. See Ref. 60 for an approximate treatment of these effects within a semi-analytical model of a Magnetized-Liner-Inertial-Fusion^{13–15} (MagLIF) implosion.
- ²⁰M. M. Basko and J. Meyer-ter Vehn, “Asymptotic scaling laws for imploding thin fluid shells,” *Phys. Rev. Lett.* **88**, 244502 (2002).
- ²¹M. Rosenbluth, R. Garwin, and A. Rosenbluth, Los Alamos Report No. LA-1850 (1954).
- ²²M. A. Leontovich and S. M. Osovets, “On the mechanism by which the current contracts in fast and intense gas discharge,” *At. Energ.* **1**, 371 (1956).
- ²³V. I. Oreshkin, “Optimization of the parameters of plasma liners with zero-dimensional models,” *Phys. Plasmas* **20**, 112505 (2013).
- ²⁴D. Potter, “The formation of high-density Z-pinch,” *Nucl. Fusion* **18**, 813 (1978).
- ²⁵It is possible to extend the present analysis of this work to include the effects of a finite rise in the current pulse. A technique based on perturbation theory is proposed in Ref. 61. Extending the present model to include this effect is left for future work.
- ²⁶T. W. Hussey, N. F. Roderick, and D. A. Kloc, “Scaling of (MHD) instabilities in imploding plasma liners,” *J. Appl. Phys.* **51**, 1452 (1980).
- ²⁷M. A. Liberman, J. S. Groot, A. Toor, and R. B. Spielman, *Physics of High-Density Z-Pinch Plasmas* (Springer, New York, NY, 1999).
- ²⁸C. Stollberg, E. Kroupp, D. Mikitchuk, P. Sharma, V. Bernsh-tam, M. Cvejić, R. Doron, E. Stambulchik, Y. Maron, A. Fruchtman, et al., “Observation of fast current redistribution in an imploding plasma column,” *Phys. Rev. Lett.* **130**, 205101 (2023).
- ²⁹H. E. Knoepfel, *Magnetic Fields: A Comprehensive Theoretical Treatise for Practical Use* (John Wiley & Sons, 2000), 1st ed.
- ³⁰S. I. Krivosheev, V. S. Pomazov, and G. A. Shneerson, “Specific features of shock wave formation in superstrong magnetic field,” *Tech. Phys. Lett.* **37**, 877 (2011).
- ³¹V. I. Oreshkin and S. A. Chaikovsky, “Stability of a nonlinear magnetic field diffusion wave,” *Phys. Plasmas* **19**, 022706 (2012).
- ³²S. A. Chaikovsky, V. I. Oreshkin, I. M. Datsko, N. A. Labet-skaya, D. V. Rybka, and N. A. Ratakhin, “Experimental study of the nonlinear diffusion of a magnetic field and skin explosion of cylindrical conductors,” *Phys. Plasmas* **22**, 112704 (2015).
- ³³V. I. Oreshkin, R. B. Baksht, S. A. Chaikovsky, R. K. Cherdizov, V. A. Kokshenev, N. E. Kurmaev, G. A. Mesyats, E. V. Oreshkin, N. A. Ratakhin, A. G. Rousskikh, et al., “Implosion of heavy metal liners driven by megaampere current pulses,” *Physics of Plasmas* **31**, 102706 (2024).
- ³⁴J. Narkis, F. Conti, and F. N. Beg, “Material effects on dynamics in triple-nozzle gas-puff Z pinches,” *Phys. Rev. E* **105**, 045205 (2022).
- ³⁵R. Nora, R. Betti, K. S. Anderson, A. Shvydky, A. Bose, K. M. Woo, A. R. Christopherson, J. A. Marozas, T. J. B. Collins, P. B. Radha, et al., “Theory of hydro-equivalent ignition for inertial fusion and its applications to OMEGA and the National Ignition Facility,” *Phys. Plasmas* **21**, 056316 (2014).
- ³⁶P. F. Schmit and D. E. Ruiz, “A conservative approach to scaling magneto- inertial fusion concepts to larger pulsed- power drivers,” *Phys. Plasmas* **27**, 062707 (2020).
- ³⁷D. E. Ruiz, P. F. Schmit, D. A. Yager-Elorriaga, C. A. Jennings, and K. Beckwith, “Exploring the parameter space of MagLIF implosions using similarity scaling. I. Theoretical framework,” *Phys. Plasmas* **30**, 032707 (2023).
- ³⁸D. A. Yager-Elorriaga, A. M. Steiner, S. G. Patel, N. M. Jordan, Y. Y. Lau, and R. M. Gilgenbach, “Technique for fabrication of ultrathin foils in cylindrical geometry for liner-plasma implosion experiments with sub-megaampere currents,” *Rev. Sci. Instrum.* **86**, 113506 (2015).

- ³⁹D. A. Yager-Elorriaga, P. Zhang, A. M. Steiner, N. M. Jordan, P. C. Campbell, Y. Y. Lau, and R. M. Gilgenbach, “Discrete helical modes in imploding and exploding cylindrical, magnetized liners,” *Phys. Plasmas* **23**, 124502 (2016).
- ⁴⁰D. A. Yager-Elorriaga, Y. Y. Lau, P. Zhang, P. C. Campbell, A. M. Steiner, N. M. Jordan, R. D. McBride, and R. M. Gilgenbach, “Evolution of sausage and helical modes in magnetized thin-foil cylindrical liners driven by a Z-pinch,” *Phys. Plasmas* **25**, 056307 (2018).
- ⁴¹S. A. Sorokin, “Fast implosion of foil liners,” *Phys. Plasmas* **26**, 082706 (2019).
- ⁴²P. C. Campbell, T. Jones, J. Woolstrum, N. Jordan, P. Schmit, J. Greenly, W. Potter, E. Lavine, B. Kusse, D. Hammer, et al., “Stabilization of liner implosions via a dynamic screw pinch,” *Phys. Rev. Lett.* **125**, 035001 (2020).
- ⁴³J. M. Woolstrum, D. A. Yager-Elorriaga, P. C. Campbell, N. M. Jordan, C. E. Seyler, and R. D. McBride, “Extended magneto-hydrodynamics simulations of thin-foil Z-pinch implosions with comparison to experiments,” *Phys. Plasmas* **27**, 092705 (2020).
- ⁴⁴S. A. Sorokin, “Magnetic implosion of thin aluminum foil liners,” *Plasma Phys. Control. Fusion* **64**, 065005 (2022).
- ⁴⁵The “asymptotically equal” symbol was used in Eqs. (19a) and (19d) since the liner outer surface technically moves inwards during the time period when the shock traverses the liner. Here, we do not take into account this small displacement. Hence, $R_{sb} \simeq R_0$.
- ⁴⁶B. Hayes, “Why w?,” *American Scientist* **93**, 104 (2005).
- ⁴⁷S. Atzeni and J. Meyer-ter Vehn, *The physics of inertial fusion: Beam plasma interaction, hydrodynamics, hot dense matter*, International series of monographs on physics (Oxford University Press Inc., New York, 2009).
- ⁴⁸M. Gersten, W. Clark, J. E. Rauch, G. M. Wilkinson, J. Katzenstein, R. D. Richardson, J. Davis, D. Duston, J. P. Apruzese, and R. Clark, “Scaling of plasma temperature, density, size, and x-ray emission above 1 keV with array diameter and mass for aluminum imploding-wire plasmas,” *Phys. Rev. A* **33**, 477 (1986).
- ⁴⁹H. R. Griem, *Principles of Plasma Spectroscopy*, Cambridge Monographs on Plasma Physics (Cambridge University Press, Cambridge, 1997).
- ⁵⁰B. Jones, C. A. Jennings, D. C. Lamppa, S. B. Hansen, A. J. Harvey-Thompson, D. J. Ampleford, M. E. Cuneo, T. Strizic, D. Johnson, M. C. Jones, et al., “A Renewed Capability for Gas Puff Science on Sandia’s Z Machine,” *IEEE Trans. Plasma Sci.* **42**, 1145 (2014).
- ⁵¹H. S. Bosch and G. M. Hale, “Improved formulas for fusion cross-sections and thermal reactivities,” *Nucl. Fusion* **32**, 611 (1992).
- ⁵²O. A. Hurricane, D. A. Callahan, D. T. Casey, E. L. Dewald, T. R. Dittrich, T. Döppner, S. Haan, D. E. Hinkel, L. F. Berzak Hopkins, O. Jones, et al., “Inertially confined fusion plasmas dominated by alpha-particle self-heating,” *Nat. Phys.* **12**, 800 (2016).
- ⁵³D. E. Ruiz, P. F. Schmit, D. A. Yager-Elorriaga, M. R. Gomez, M. R. Weis, C. A. Jennings, A. J. Harvey-Thompson, P. F. Knapp, S. A. Slutz, D. J. Ampleford, et al., “Exploring the parameter space of MagLIF implosions using similarity scaling. II. Current scaling,” *Phys. Plasmas* **30**, 032708 (2023).
- ⁵⁴D. E. Ruiz, P. F. Schmit, M. R. Weis, K. J. Peterson, and M. K. Matzen, “Exploring the parameter space of MagLIF implosions using similarity scaling. III. Rise-time scaling,” *Phys. Plasmas* **30**, 032709 (2023).
- ⁵⁵S. A. Slutz, M. C. Herrmann, R. A. Vesey, A. B. Sefkow, D. B. Sinars, D. C. Rovang, K. J. Peterson, and M. E. Cuneo, “Pulsed-power-driven cylindrical liner implosions of laser preheated fuel magnetized with an axial field,” *Phys. Plasmas* **17**, 056303 (2010).
- ⁵⁶M. R. Gomez, S. A. Slutz, P. F. Knapp, K. D. Hahn, M. R. Weis, E. C. Harding, M. Geissel, J. R. Fein, M. E. Glinsky, S. B. Hansen, et al., “Assessing stagnation conditions and identifying trends in Magnetized Liner Inertial Fusion,” *IEEE Trans. Plasma Sci.* **47**, 2081 (2019).
- ⁵⁷D. A. Yager-Elorriaga, M. R. Gomez, D. E. Ruiz, S. A. Slutz, A. J. Harvey-Thompson, C. A. Jennings, P. F. Knapp, P. F. Schmit, M. R. Weis, T. J. Awe, et al., “An overview of magneto-inertial fusion on the Z machine at Sandia National Laboratories,” *Nucl. Fusion* **62**, 042015 (2022).
- ⁵⁸O. A. Hurricane, D. T. Casey, O. Landen, A. L. Kritcher, R. Nora, P. K. Patel, J. A. Gaffney, K. D. Humbird, J. E. Field, M. K. G. Kruse, et al., “An analytic asymmetric-piston model for the impact of mode-1 shell asymmetry on ICF implosions,” *Phys. Plasmas* **27**, 062704 (2020).
- ⁵⁹D. E. Ruiz, “Degradation of performance in ICF implosions due to Rayleigh–Taylor instabilities: a Hamiltonian perspective,” accepted in *Phys. Plasmas* (2024).
- ⁶⁰R. D. McBride and S. A. Slutz, “A semi-analytic model of magnetized liner inertial fusion,” *Phys. Plasmas* **22**, 052708 (2015).
- ⁶¹D. D. Ryutov and M. A. Dorf, “Evolution of helical perturbations in a thin-shell model of an imploding liner,” *Phys. Plasmas* **21**, 112704 (2014).